Influence of support pore size and porosity on epoxide-based TFC membranes

Nathalie Lenaerts[a], Rhea Verbeke[a], Douglas M. Davenport[a], Scout Caspers[a], Samuel Eyley[b], Karim-Alexandros Kantre[c], Alexander Volodine[d], Ricardo Helm[e], Maik Butterling[f], Maciej Oskar Liedke[f], Andreas Wagner[f], Wim Thielemans[b], Johan Meersschaut[c], Marcel Dickmann[e], Ivo F.J. Vankelecom[a*]

[a]*Membrane Technology Group (MTG), Division cMACS, Faculty of Bioscience Engineering, KU Leuven, 3001 Leuven, Belgium*
[b]*Sustainable Materials Lab, Department of Chemical Engineering, KU Leuven, Kortrijk, Belgium*
[c]*Imec, Leuven, Belgium*
[d]*Laboratory of Solid-State Physics and Magnetism, KU Leuven, Leuven, Belgium*
[e]*Institut für Angewandte Physik und Messtechnik, Universität der Bundeswehr München, 85577 Neubiber, Germany*
[f]*Institute of Radiation Physics, Helmholtz-Zentrum Dresden-Rossendorf, Dresden, Germany*

[*]*Corresponding author: ivo.vankelecom@kuleuven.be*

Highlights

- Support layer properties are critical to tune the epoxide-based TFC membrane permeance.
- Pore size (20 – 90 nm) and surface porosity (4 – 10%) of the support do not affect selectivity.
- Larger pores result in higher permeances, probably due to the funnel effect.
- The solvent used during support layer preparation via phase inversion affects the TFC membrane performance.
- The post-treated poly(epoxyether) TFC membranes achieve ~65% NaCl rejections with a water permeance of ~8 L m^{-2} h^{-1} bar^{-1}.

Graphical abstract

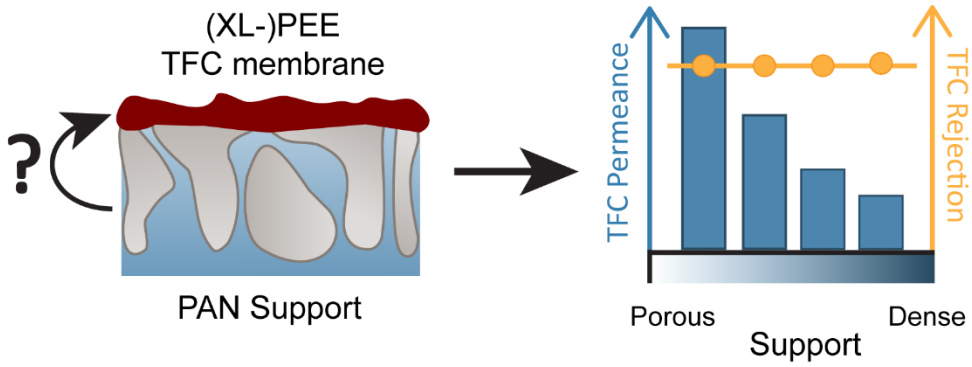

Abstract

The drive to expand the implementation of membrane separation technology towards harsher environments prompted the development of chemically robust epoxide-based TFC membranes. This

work seeks to better understand the influence of the support on epoxide-based TFC membrane performance and properties. More specifically, it investigates the impact of porous PAN support layers of different porosities and pore sizes on the formation of poly(epoxyether) (PEE) thin films via interfacial initiation of polymerization (IIP), and their more cross-linked and more charged counterparts PEE (XL-PEE) arising from a subsequent post-treatment step. A systematic study was conducted using a series of supports with pore sizes varying from 20 nm to 90 nm and porosities in the range of 4% to 10%, while maintaining identical synthesis conditions for the selective layer. The physicochemical properties of the selective layer were characterized in-depth with X-ray photoelectron spectroscopy (XPS), elastic recoil detection (ERD), transmission electron microscopy (TEM), positron annihilation lifetime spectroscopy (PALS), and atomic force microscopy (AFM) to elucidate the synthesis-structure-performance relationship. PEE TFC membranes comprising these supports had a broad range in water permeances of 5 – 30 L m^{-2} h^{-1} bar^{-1} with consistent methyl orange (327 g mol^{-1}) rejections of ca. 90%. The densified XL-PEE TFC membranes all achieved ca. 65% NaCl rejections, again independent of the support properties. In contrast, more porous supports resulted in more permeable TFC membranes, which can be attributed to the so-called funnel effect. Additionally, the solvent used to prepare the support layers through non-solvent induced phase separation also impacted the selective layer by affecting the interfacial properties during IIP. This work thus demonstrates that the support can serve as an easy tool to fine-tune the performance of the next-generation of high-performance epoxide-based TFC membranes.

Keywords

Nanofiltration; TFC membranes; Epoxide-based membranes; PAN support; Interfacial initiation of polymerization

1. Introduction

Water scarcity poses a global challenge, which threatens the sustainability of our society and has a profound impact on our ecosystems. The growing concern for adequate water supply, and the constrained accessibility of natural resources, drive the rapid development of water treatment facilities [1–3]. By promoting water reuse and thus integrating circular economy principles, these approaches address waters scarcity while minimizing environmental impacts [4–6]. In addition, desalination of seawater and brackish water with nanofiltration (NF) and reverse osmosis (RO) membranes have proven to be viable strategies to mitigate water scarcity globally [5].

Conventional NF and RO membranes are thin-film composite (TFC) membranes, comprising a thin, dense, cross-linked polyamide (PA) selective layer prepared through interfacial polymerization (IP) on top of a porous support. Its exceptional water-salt perm-selectivity and the ability to optimize the support and selective layer individually, position PA as the gold standard for NF and RO applications [7–9]. Despite its widespread implementation on industrial scale [10], PA-based membranes degrade during long-term operation at low and high pH. Furthermore, the inherent susceptibility for cleavage of the PA bonds, when exposed to oxidizing agents during membrane cleaning cycles, necessitate extensive (de)chlorination pretreatment [11]. Hence, commercial membranes need to be replaced regularly, decreasing plant productivity, and significantly increasing overall process cost and lowering sustainability [11–14]. In addition, there is increasing interest to use membrane technology in industrial applications operating under harsh pH (*i.e.*, pH<2 and pH>11), *e.g.*, treatment of acid mine leachates, in flow batteries, for lithium recovery, and in food and bioprocess applications to allow more intense or cheaper cleaning [9,13].

This quest for chemically robust membranes leads to the introduction of emerging polymer chemistries, such as polyamines [15–17], polyurea [18], polyelectrolyte membranes [19,20], and the recently developed epoxide-based membranes [21–23]. The exceptional chemical, mechanical, and thermal stability of epoxide resins inspired the development of these chemically robust membranes.

Instead of the well-known epoxide bulk polymerization, this system was transferred to an interfacial synthesis system, to obtain an epoxide-based selective layer [22,24], and to a non-solvent induced phase separation (NIPS) protocol to obtain integrally skinned asymmetric membranes [25,26], as such establishing a new platform chemistry for membrane synthesis. For the interfacial system, a tertiary amine-induced ring opening polymerization (ROP) of the reactive oxirane ring results in a thin, yet selective layer consisting of a poly(epoxyether) (PEE) network. The first generation of the PEE membranes was synthesized from an aqueous solution with a bifunctional tertiary amine and tetrafunctional epoxide monomer dissolved in toluene. The obtained PEE TFC membranes only had a NaCl rejection of ~20% and water permeance of 8 L m^{-2} h^{-1} bar^{-1} [21,22]. To achieve the desired salt rejection for desalination applications, an additional post-treatment step was introduced by re-exposing the formed PEE selective layer to solutions containing the epoxide monomer and the amine. This extra step resulted in more quaternary ammonium (QA) incorporation, creating a more positively charged and a more cross-linked PEE (XL-PEE) selective layer [23,27]. The high tunability of this novel polymer chemistry has already been demonstrated by screening a variety of initiators and epoxide monomers, at varying concentrations, to create NF membranes with a wide range of performances [27].

It has been shown for conventional PA-based TFC membranes that the support plays a crucial role in defining the synthesis-structure-performance (SSP) relationship [28–31]. The support surface chemistry (*i.e.*, hydrophilicity), roughness and pore properties (*e.g.,* surface porosity, pore sizes and pore size distributions) partially determine the nanoscale PA characteristics and salt selectivity [28,31,32]. For instance, it is demonstrated that the amine supply, *i.e.*, diffusion of the amine toward the reaction zone, strongly influences the rate of polymerization and thus the degree of cross-linking [33,34]. Furthermore, the pore structure dictates the susceptibility of the formed film to penetrate into the pore itself, impacting the thickness and roughness of the PA film [29]. In addition, the typical ridge-and-valley morphology of the PA selective layer is also related to the support properties, where theoretical frameworks such as nanofoaming, confinement effects, Marangoni convection, 'volcano-like eruption' models, heat dissipation differences and instability mechanisms try to further elucidate the interplay between the porous support and the selective layer [30,31,35–37]. Despite the large amount of literature available on support studies for PA-based TFC membranes, contradicting results are often reported [30]. This, combined with the fact that the very fast self-limiting polycondensation reaction of the PA system is very different from the much slower anionic ring opening polymerization reaction of the epoxide system, indicates that the general conclusions for PA cannot be transferred to epoxide-based TFC membranes. Therefore, a systematic study, investigating the influence of pore properties of the support layer on a epoxide-based selective layer, will contribute to understanding the SSP relationship of these IIP membranes.

In this work, a selection of polyacrylonitrile (PAN) based supports with a variety of pore sizes and surface porosities, prepared via NIPS, was used to critically assess the influence of the support on the performance and physicochemical properties of the PEE and XL-PEE TFC membranes. The formation mechanism and nanoscale properties of the selective layers were investigated through extensive characterization via scanning electron microscopy (SEM), elastic recoil detection (ERD), X-ray photoelectron spectroscopy (XPS), transmission electron microscopy (TEM), atomic force microscopy (AFM) and positron annihilation lifetime spectroscopy (PALS), as well as filtration experiments. The gained insights of the support–selective layer interplay led to a better understanding of the SSP relationship of IIP membranes. These insights will help to predict the performance, and in turn increase the efficiency of designing future epoxide-based TFC membranes.

2. Materials and methods

2.1 Materials

The epoxide monomer tetraphenolethane tetraglycidyl ether (EPON™ Resin 1031, further denoted as EPON, Hexion) and the initiator *N,N,N',N'*-tetramethyl-1,6-hexanediamine (TMHD, 99%, Acros Organics™) were used as received. For the lab-synthesized polyacrylonitrile (PAN) supports, polyester non-woven Hollytex 3329 (Kavon Filter Products Co.) and PAN (MW of 150 000 g mol^{-1}, Scientific Polymer Products) were used. The following solvents were used for membrane synthesis: toluene (99+%, extra pure, Acros Organics™), *N*-methyl-2-pyrrolidone (NMP, 99%, Acros Organics™), *N,N'*-dimethylformamide (DMF, anhydrous, 99+%, Fischer Scientific), dimethyl sulfoxide (DMSO, 99.9+%, Alpha Aesar) and Milli-Q (MQ) water (18.2 MΩ.cm at 25 °C). 2-propanol (IPA, ≥99.5%, Sigma-Aldrich) was used to rinse the supports as pre-treatment prior to the TFC membrane synthesis. Sodium chloride (NaCl, ChemLab) and methyl orange (MO, Fluka Chemicals) were used as solutes during filtration experiments. For gas-liquid porosimetry measurements, a fluorinated hydrocarbon wetting fluid (Porefil 250, Porometer), ethanol (99+%, Fisher Scientific) and *n*-pentane (99+%, Fisher Scientific) were used. Ethanol (ChemLab) and LR White resin (hard cure, Ted Pella, Inc., Redding, USA) were used for TEM.

2.2 Methods

2.2.1 Preparation of PAN support

The supports were prepared by dissolving 12 – 17 wt% of PAN (polymer powder dried overnight at 100 °C) in a solvent (DMSO, NMP or DMF) at 60 °C, after which it was degassed in the vacuum oven for 2 h at 25 °C. Prior to casting the solutions, the non-woven was impregnated with the same solvent as that of the casting solution, and dabbed to remove any excess solvent. The polymer solution was then cast using an automatic casting knife (MEMCAST™, Porometer, Belgium) with a constant speed of 0.2 cm s^{-1} at room temperature (25 °C) and a thickness of 250 µm on top of the impregnated non-woven. After 20 s, the cast polymer film was immersed for 20 min in a coagulation bath containing deionized water. The synthesized support was then stored in deionized water at 4 °C until further use. In order to assess the impact of solvents used during the selective layer formation, solvent annealing of the PAN support was performed by mimicking the synthesis steps of the XL-PEE selective layer without initiator or epoxy monomers present, as described previously [21]. When explicitly mentioned, a wash step of 25 v/v% IPA in deionized water for 30 min followed by three times rinsing with deionized water for 30 min, was introduced to remove the residual solvent trapped in the polymer matrix of the support after phase inversion.

2.2.2 Synthesis of epoxide-based selective layer

Similar to previous work [23], epoxide-based selective layers were synthesized via interfacial initiation of polymerization (IIP) (**Figure 1**). First, the porous PAN support was immersed in a 1.0 w/v% aqueous TMHD solution for 1 h. Excess solvent was removed with compressed air whereafter the support (active area of 88 cm^2) was fixed in a customized IIP set-up with the skin layer facing up. 40 mL of a 1.5 w/v% EPON in toluene solution was poured on the support. After a reaction time of 1 h, the toluene solution was discarded. For the PEE membranes, the membrane surface was rinsed with toluene to remove unreacted compounds, and then allowed to air-dry for 10 min followed by storage in deionized water at 4 °C until further use. For the XL-PEE membranes, no toluene rinse was performed. Instead, 40 mL of fresh 1.5 w/v% EPON solution in toluene was added and allowed to react for 1 h, followed by a rinse with toluene. Then, 40 mL of 1.0 w/v% aqueous solution of the initiator was poured on the PAN support. After 1 h reaction time, the solution was discarded and the synthesized XL-PEE membrane was washed with toluene and air-dried for 10 min, followed by storage in deionized water at 4 °C until further use.

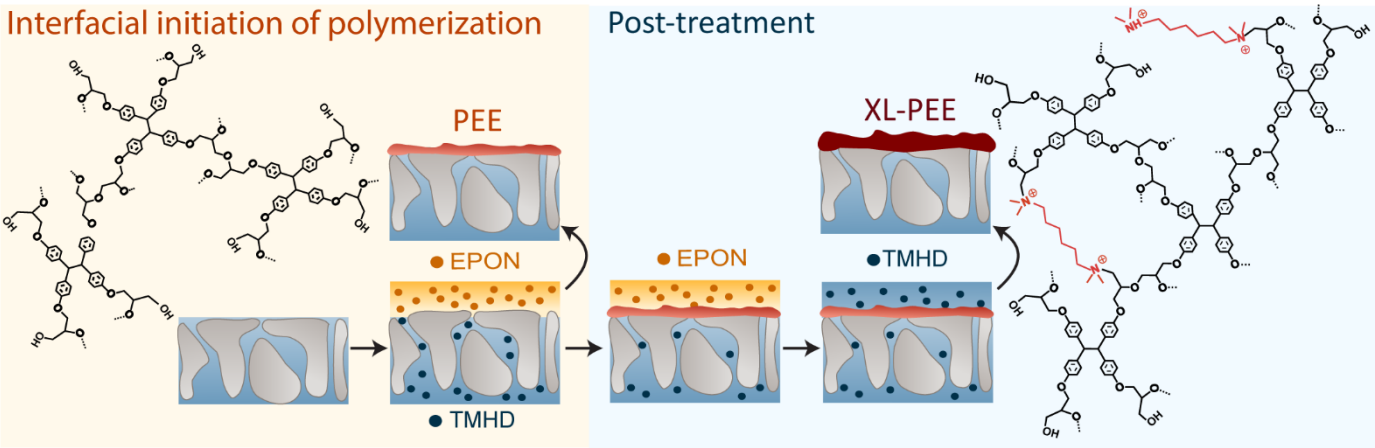

Figure 1. Synthesis scheme for the PEE and the XL-PEE TFC membranes, as described in previous work [23]. Via IIP on a PAN support impregnated with a TMHD in water solution and an EPON in toluene solution, a PEE selective layer is formed on top of the porous support. Via a two-step post-treatment process, where sequentially a fresh EPON solution, a toluene rinse and a fresh diamine solution are applied, a XL-PEE selective layer is obtained [23].

2.2.3 Membrane performance

A high-throughput dead-end filtration apparatus was used to determine the performance of the PAN supports, PEE and XL-PEE membranes. Filtration experiments at room temperature of the supports (pristine and annealed) and the TFC membranes were done at 1 bar and 10 bar, respectively, and stirred at 350 rpm to minimize concentration polarization. MQ water was used as the feed solution for the support layers and TFC membranes, while aqueous solutions of 5 mM NaCl or 35 µM MO (327.33 g mol^{-1}) were also used for the TFC membranes. MO and NaCl were used as solute for the PEE TFC membranes, while only NaCl was used as solute for the XL-PEE TFC membranes, as the post-treatment step improves NaCl rejection significantly.

The pure water permeance, expressed as pure water permeability coefficient, A (L m^{-2} h^{-1} bar^{-1}), when no solutes were used, was calculated using Eq. 1:

$$A = \frac{V}{A_m \, t \, \Delta P} \qquad Eq.1$$

where V (L) is the permeate volume, A_m (m^2) is the membrane area (*i.e.*, 1.54 cm^2), t (h) is the filtration time, and ΔP (bar) is the applied pressure.

The observed membrane rejection, R_{obs} (%), of NaCl and MO was calculated using Eq. 2:

$$R_{obs} = 100 \times \left(\frac{C_f - C_p}{C_f}\right) \qquad Eq.2$$

where C_f and C_p are the bulk solute concentrations in the feed and permeate, respectively, measured with a Consort C3010 multiparameter analyzer for filtrations with NaCl, or a Shimadzu UV-1800 UV-Vis spectrophotometer (at 464 nm) for MO filtrations.

The real rejection, R_{real} (%), which is an intrinsic parameter of the selective layer, was estimated by accounting for concentration polarization (CP) using film theory, according to the formula [38,39]:

$$R_{real} = 100 \times \left(\frac{C_m - C_p}{C_m}\right) = 100 \times \frac{C_p}{c_f \exp\left(\frac{J_w}{k_f}\right) - c_p\left(\exp\left(\frac{J_w}{k_f}\right) - 1\right)} \qquad Eq.3$$

where C_m and C_p are the solute concentrations at the feed side of membrane surface and in the bulk permeate, respectively. J_w is the measured water flux and k_f is the mass transfer coefficient, which is estimated based on the Sherwood correlations (**Supplementary materials: section 1** and **2**) [40]. Note

that these filtrations were performed on a dead-end filtration apparatus with one feed solution for multiple membrane coupons. Standard deviations are based on three to five replicates to include the heterogeneity of the membrane samples.

2.2.4 Membrane physicochemical characterization

2.2.4.1 Attenuated Total Reflectance Fourier-Transform Infrared (ATR-FTIR)

ATR-FTIR was used to determine the membrane chemical composition. Spectra of the different supports (pristine and annealed) as well as the PEE and XL-PEE TFC membranes were taken with a Bruker Alpha spectrometer, equipped with a diamond crystal. 32 scans at a resolution of 4 cm^{-1} in the range of 400 – 4000 cm^{-1} were taken. The samples were dried at room temperature prior to analysis.

2.2.4.2 X-ray photoelectron spectroscopy (XPS)

XPS was performed to determine the elemental composition of the membrane surface. Spectra were recorded on a Kratos Axis Supra photoelectron spectrometer using a monochromated Al Kα (1486.7 eV, 120 W) X-ray source, hybrid (magnetic/electrostatic) optics and a hemisphere analyzer. The analyzer was operated in fixed analyzer transmission mode with a pass energy of 160 eV for survey spectra and 20 eV for high resolution spectra. Binding energy was referenced to aromatic C-C at 284.7 eV. Spectra were processed in CasaXPS (v 2.3.26). Quantification was performed using relative sensitivity factors based on Scofield photoelectron cross-sections and corrected for the electron attenuation length [41]. The instrumental transmission characteristics were corrected using an NPL transmission function [42]. The resulting composition does not consider any surface nanostructure and should be considered the homogeneous equivalent composition.

2.2.4.3 Scanning electron microscopy (SEM)

SEM images were recorded using a JEOL JSM-6010 LV SEM operated at an acceleration voltage of 10 kV to obtain top-view and cross-view images. The samples were sputtered with a 60/40 Au/Pd coating using a JEOL JFC-1300 Auto Fine Coater. The membrane samples were air-dried prior to sample preparation.

2.2.4.4 Gas-liquid porosimetry (GLP)

GLP was used to determine the mean pore size and pore size distribution of the supports using a POROLUX™ 1000 system (Porometer, Belgium). To avoid pore collapse, membrane coupons (25 mm diameter) were first immersed for 15 min in different solvents: deionized water, 1:1 v/v% deionized water/ethanol, ethanol, 1:1 v/v% ethanol/*n*-pentane and *n*-pentane, after which they were dried under ambient conditions for at least 1 h. Then, the membranes were immersed in the wetting liquid Porefil® (surface tension of 1.6×10^{-3} N m^{-1}) and placed under vacuum for at least 30 min before measurements were taken. A stepwise pressure scan was performed to gradually displace the wetting liquid with N_2, while recording the pressure and the corresponding gas flow rate. Solvent removal from the pores at increasing pressure is governed by the Young-Laplace equation (Eq. 4):

$$\mathrm{P} = \frac{4\,\gamma\,\cos\Theta}{d} \qquad Eq.\,4$$

where *P* is the pressure (Pa), *γ* is the surface tension (N m^{-1}), *d* is the pore diameter (m), and *Θ* is the contact angle (°). Estimations of the pore numbers, surface porosity, and pore size distribution were obtained via a modified Hagen-Poiseuille formula and Darcy equations through the Porometer software (version 3.13 GUI). For the 17 wt% PAN support synthesized using NMP, results are based on an extrapolation of the measured data to higher pressures, due to incomplete removal of the wetting liquid caused by a mechanical limitation of the porometer equipment.

2.2.4.5 Elastic recoil detection (ERD)

ERD was used for a selection of PEE and XL-PEE TFC membrane samples to obtain the elemental depth-profile and to estimate the thickness of the selective layer. A 6SDH tandem accelerator with a maximum terminal voltage of 2.0 MV from National Electrostatics Corporation (Middleton, WI, USA)

was used to perform Time of Flight-Energy (ToF-E) ERD measurements. A primary ion beam of 8.016 MeV $^{35}Cl^{4+}$ was used. The ToF-E detector was at 40° with respect to the beam direction. The ion beam was impinging on the sample at a glancing angle of 12°. To reduce the beam induced damage to the selective layer, samples were moved over a range of 30 mm during the measurement. The data acquisition time per sample was 2400 s. For the PEE films, the thickness was determined by considering the entire film signal. For the XL-PEE membranes, the probing depth was not high enough to reveal the entire oxygen distribution. In this case, the film thickness was estimated from the depth at which the O and N atomic fractions intersect [23]. The ERD results are expressed as atomic fractions and areal densities (atoms cm^{-2}). In the present work, the conversion from the areal density to a physical thickness (nm) was done by assuming a mass density of 1 g cm^{-3} [23,24]. The uncertainty on the thickness obtained from the ERD analysis is believed to be dominated by the assumption of the mass density as well as the surface roughness.

2.2.4.6 Transmission electron microscopy (TEM)

TEM measurements were performed to estimate the thickness of the selective layer and gain more insight in the nanoscale structure. First, a solvent exchange of the wet membrane samples with ethanol was done for 15 min and repeated three times, followed by a solution of 1:1 v/v% ethanol/resin solution for 1 h, which was followed by a 1:2 v/v% ethanol/resin solution for 2 h. Next, the samples were immersed in two sequential exchanges of pure resin for 3 h and approximately 20 h, respectively. Afterwards, the samples were transferred to embedding capsules, filled with the resin, and cured at 65 °C under vacuum for approximately 14 h. After curing, 100-nm-thick cross-sections were prepared with a diamond knife (3 mm Ultra 35°, Diatome) using a Leica Ultramicrotome UCT (Leica Microsystems GmbH, Germany) and mounted onto formvar/carbon coated copper grids (Electron Microscopy Sciences). Annular Dark Field (ADF) images (at 20 kx, 30 kx, 40 kx, 50 kx, 60 kx and 80 kx) in STEM mode were obtained using an ARM200F TEM (JEOL). The selective layer thickness was determined based on at least 3 measurements using DigitalMicrograph software [23].

2.2.4.7 Positron annihilation lifetime spectroscopy (PALS)

Variable energy positron annihilation lifetime spectroscopy (VEPALS) measurements were conducted at the Mono-energetic Positron Source (MePS) beamline at Helmholtz-Zentrum Dresden-Rossendorf (Germany) to determine the free-volume element (FVE) size and their abundance in the PEE and XL-PEE selective layers [43]. A $CrBr_3$ scintillator coupled to a Hamamatsu R13089-100 photomultiplier tube was used for gamma quanta acquisition and the signals were processed by the SPDevices ADQ14DC-2X digitizer [44]. The time resolution was in the range of 0.240 ns (full width at half maximum). The resolution function required for the analysis of the spectra includes a sum of several Gaussian functions with distinct intensities and relative shifts, both depending on the positron implantation energy. It was determined by the measurement and analysis of a reference sample, *i.e.*, amorphous Yttria-stabilized zirconia, which exhibited well-known lifetime components. All measured lifetime spectra contained at least 1×10^7 counts. Positron implantation energies of 0.7, 1 and 1.2 keV were used to measure FVEs at a median implantation depth of ~15 nm, 28 and 38 nm, respectively, assuming a polymer density of 1 g cm^{-3} [23]. The best-fitting results were obtained for all samples via a Levenberg-Marquard fitting algorithm with the simplest multi-exponential model, *i.e.,* four lifetime components: *p*-Ps, free e^+, *o*-Ps_{short} (τ_3), and *o*-Ps_{long} (τ_4). A reduced X^2 value of less than 1.2 was achieved for all fits. The overall fit variances were below 1.2 for all samples. The intensity-weighted average of the o-Ps lifetime was directly correlated to the FVE size according to the Tao-Eldrup model, assuming spherical holes [45].

2.2.4.8 Atomic Force microscopy (AFM)

AFM measurements were performed to measure the roughness of the selective layer in tapping mode, using SSS-FMR probes from NanoAndMore GmbH (Germany) at ambient conditions using a Dimension 3100D AFM (Bruker). The cantilever was made from silicon with a spring constant of 2.3 N m^{-1} and a nominal tip apex radius of < 2 nm. AFM measurements were performed over scan areas of 1 × 1 μm^2

in at least three different locations for each of the samples. The AFM images were flattened with a first order flattening protocol after scanning, whereafter the root-mean-squared (RMS) roughness was calculated using the ISO 25178-2 standard [46].

3. Results and discussion

3.1 Tuning support properties via PAN concentration in casting solution

The supports prepared from different PAN concentrations in the casting solution result in membranes with similar morphology, *i.e.*, small asymmetric macrovoids near the skin layer and large finger-like macrovoids in the bottom part (**Figure 2**), which was also observed previously [47]. Moreover, the different supports clearly demonstrate the expected trade-off between polymer concentration and pure water permeance, as the permeance dropped from ~ 1400 L m^{-2} h^{-1} bar^{-1} to ~ 50 L m^{-2} h^{-1} bar^{-1} when increasing the polymer concentration from 12 wt% to 17 wt% PAN in NMP (**Figure 3a**). The increased polymer concentration in the support casting solutions affects the pore density of the skin-layer, as demonstrated by the porosimetry data (**Figure 3b**). Namely, the mean pore size and the total pore area decreased with increasing polymer concentration, in agreement with the obtained permeance data (**Figure 3a**). No substantial impact of solvent annealing is observed for most supports, although there is a slight increase for the highest and lowest PAN concentrations. However, the permeances did not drop as significantly as noticed previously for polyimide-based supports [21] and hence, the PAN layer is not expected to significantly contribute to the overall rejection of the PEE and XL-PEE membranes.

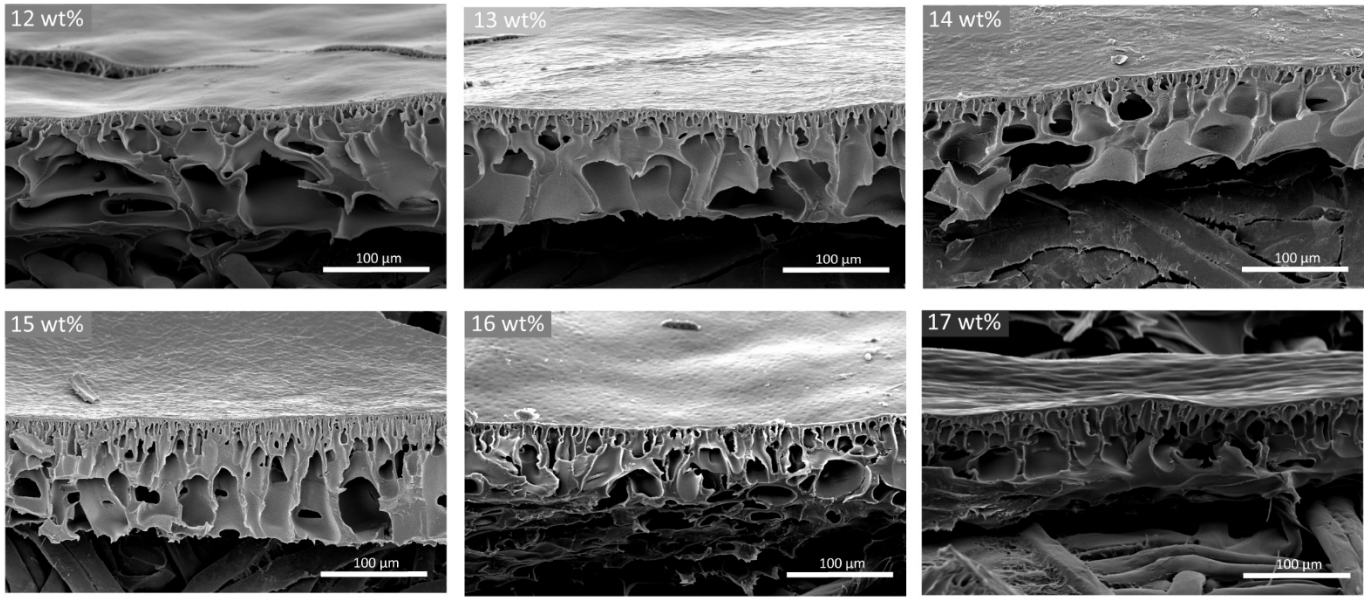

Figure 2. Cross-view SEM images of pristine support layers (12 – 17 wt% PAN in NMP).

3.1.1 Effect of support on PEE selective layer

PEE TFC membranes with TMHD as initiator and EPON as monomer were successfully synthesized on each support layer (12 – 17 wt% PAN in NMP), as demonstrated by the significant drop in water permeance below 30 L m^{-2} h^{-1} bar^{-1} and real MO rejections of approximately 90% for all PEE TFC membranes (**Figure 3c**). Interestingly, despite having a significant effect on the water permeance, the support porosity does not seem to affect the selectivity, not even for the 12 wt% membrane, which also has a 90% MO rejection and a high permeance of 27 L m^{-2} h^{-1} bar^{-1}. Conversely, an inverse correlation between the PAN concentration in the support and the water permeance of the PEE membranes is observed (**Figure 3a** and **c**). In contrast to the state-of-the-art PA TFC membranes, the pore properties of the support thus do not contribute significantly to the selectivity of the PEE

membranes under the employed synthesis conditions [30]. Consequently, the performance of these PEE TFC membranes deviates from the typical water–salt perm-selectivity trade-off [48].

Possibly, a more porous support (*i.e.,* prepared from a low PAN concentration) could contribute to a more open 3D PEE network, as larger pores may result in a higher supply of TMHD toward the reaction zone. This in turn may cause more ROP initiation during chain-growth polymerization, resulting in shorter PEE chains, hence in a lower mass density of the formed film, and thus in higher permeances [49]. This is in contrast to PA membranes synthesized via step-growth polymerization on a porous support, where an increase in amine (*i.e.*, *m*-phenylene diamine) supply results in a higher cross-linking degree [30]. Provided this hypothesis for the PEE membranes is valid and assuming MO rejection is mostly based on size-exclusion, an increasing trend in MO rejection would be expected with increasing PAN concentration. However, since the real rejection, R_{real}, which is an intrinsic parameter of the selective layer [40,50], remains constant for the entire range of support layers for both MO and NaCl (**Figure 3c**), the selective layer should be identical for the different supports. To investigate the cause of the difference in observed water permeance with increasing PAN, but not in the real MO rejection, the physicochemical properties of the PEE selective layers were further studied in detail.

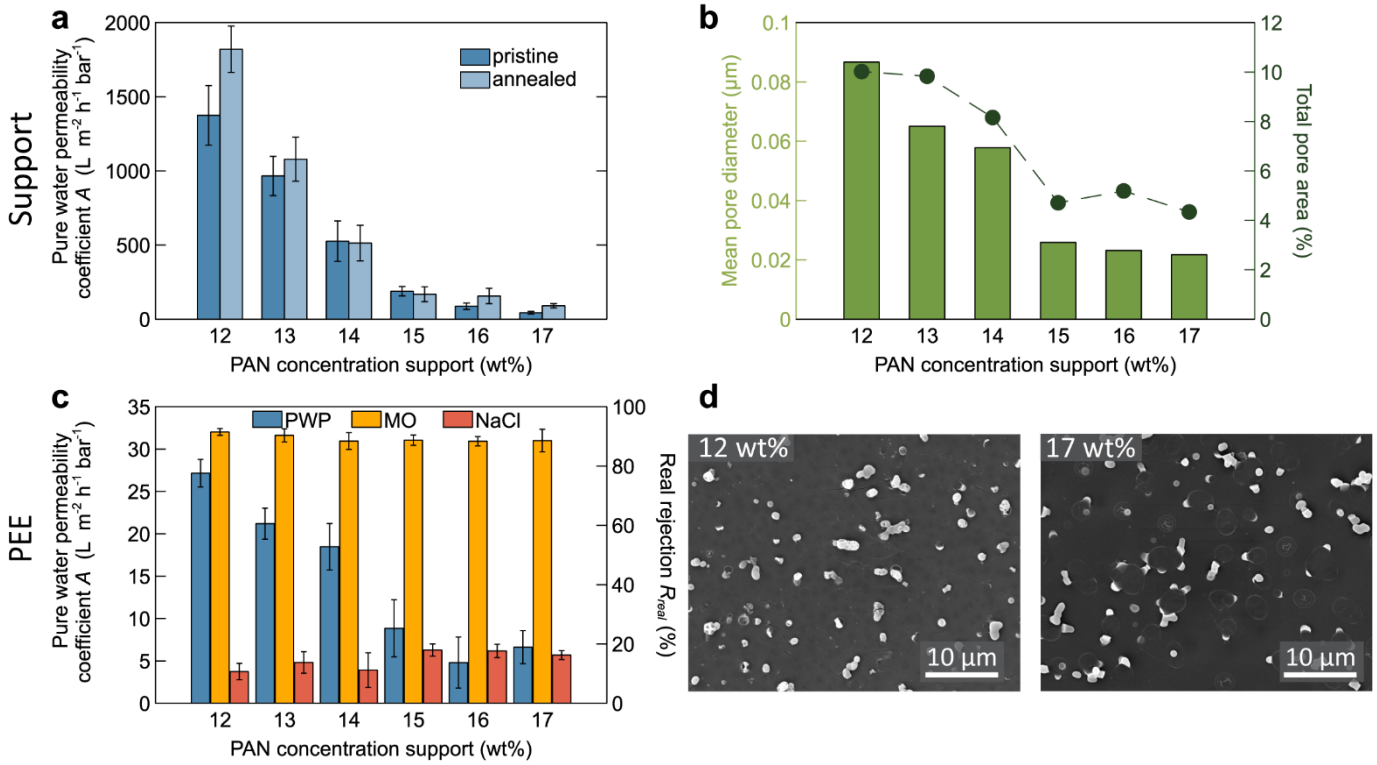

Figure 3. (a) Pure water permeance, expressed as pure water permeability coefficient, *A*, of pristine and annealed supports synthesized from 12-17 wt% PAN in NMP via NIPS (annealing was performed without the presence of the initiator and the epoxide monomer). Experimental filtration conditions: 25 °C, 1 bar, MQ water. **(b)** Mean pore diameter and total pore area derived from porosimetry measurements of the pristine support layers synthesized from 12-17 wt% PAN in NMP. **(c)** Pure water permeance, expressed as the pure water permeability coefficient *A*, MO rejection and NaCl rejection of the PEE TFC membranes as a function of the support layer PAN concentration. Experimental filtration conditions: 25 °C, 10 bar, 35 µM aqueous MO solution and 5 mM aqueous NaCl solution. **(d)** SEM images of PEE TFC membranes synthesized on 12 and 17 wt% PAN in NMP supports.

PALS measurements were performed to determine the difference between the size of free volume elements (FVEs) of the PEE fabricated on the 12 and 17 wt% PAN support layers. However, no clear differences could be observed in the size of FVEs between the different PEE TFC membranes. The relative abundance of the FVEs is also rather constant for different supports, and comparable to state-of-the-art NF membranes (**Table 1** and **Figure S2**) [51,52]. Additionally, as the support supplies TMHD

to the interface, a more porous support can therefore have more incorporation of QA groups in the selective layer (cfr. hypothesis above). However, the obtained XPS data (**Table 1**) shows a similar QA content (approximately 0.3 at.%) in the upper ca. 5 – 10 nm of the selective layer (*i.e.*, the measurement depth of XPS) for the PEE layer on top of the 12 and 17 wt% PAN support [21]. Top-view SEM images do not show a significant difference in the typical protruding structures for the epoxide-based selective layers and also do not seem related to the porosity or pores of the support (**Figure 3d** and **S3**). These results thus confirm that the selective layer formation is independent of the support and is in agreement with the results for real rejection, R_{real}. As a consequence, the decrease in water permeance must be related to other film properties or transport mechanisms. Moreover, it highlights the difference in selective layer formation between PA and these PEE thin films, and more generally between IP and IIP, where differences in pore sizes and porosities result in different selective layer morphologies and cross-linking degrees.

Table 1. Quantitative overview of physicochemical characterization (PALS, XPS, ERD, TEM and AFM) on PEE and XL-PEE TFC membranes, synthesized on supports made with 12 and 17 wt% PAN in NMP. Extra information is available in the Supplementary materials (**Figure S2** and **S4** and **Table S2-S6**). The PALS data depicted in this table were obtained from an intensity-weighted average of τ_3 and τ_4 and obtained at an implantation energy of 1 keV. For TEM, N.M. indicates "not measurable" due to insufficient contrast between selective layer and support. **Figure S7** shows the large protrusions on the selective layer, hence the large standard deviations for 12 and 17 wt% XL-PEE.

TFC membrane	Characterization					
	PALS		XPS	ERD	TEM	AFM
	Size FVEs (Å)	Abundance FVEs (%)	R_4N^+ (at.%)	Thickness (nm)	Thickness (nm)	RMS (nm)
12 wt% PEE	4.8	17.99	0.30 ± 0.03	55	N.M.	5.9 ± 0.41
17 wt% PEE	4.8	18.17	0.29 ± 0.08	64	N.M.	7.49 ± 4.33
12 wt% XL-PEE	4.4	19.81	1.38 ± 0.15	338	121 ± 46	2.55 ± 0.27
17 wt% XL-PEE	4.8	15.38	1.51 ± 0.33	411	143 ± 145	2.51 ± 0.50

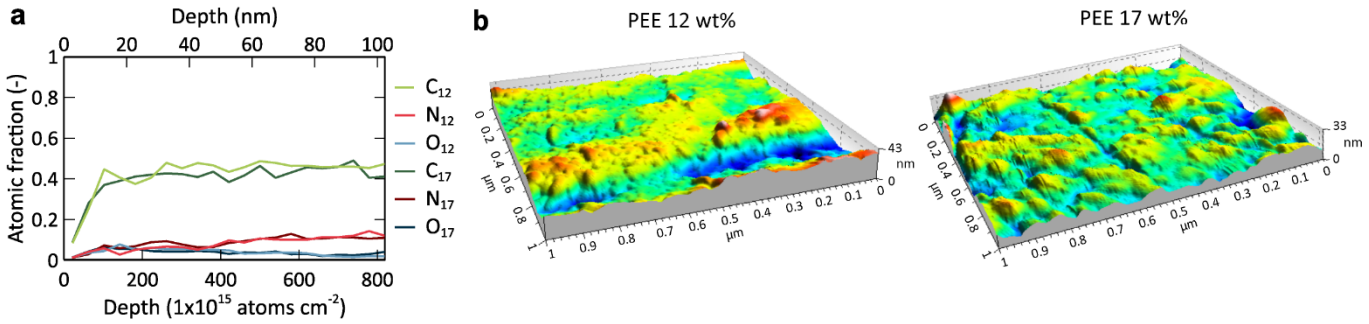

Figure 4. (a) ERD on the PEE TFC membranes for the support layers synthesized with 12 and 17 wt% in NMP. **(b)** AFM images with a scan range of 1 × 1 μm² of the PEE TFC membranes synthesized on 12 and 17 wt% PAN in NMP.

To further investigate the role selective layer thickness and roughness might play in the observed permeance trend, the selective layers synthesized on the most and least porous supports, were measured via ERD, TEM, and AFM. ERD measurements show that the PEE layer on the more porous support is marginally thinner, *i.e.,* 55 nm for 12 wt% compared to 64 nm for 17 wt% PAN support (**Table 1** and **Figure 4a**). TEM imaging of the PEE TFC membrane was inconclusive as it was difficult to distinguish between the skin-layer of the support and the actual PEE selective layer (**Figure S4**), as previously observed [23]. However, TEM depicted a rather homogeneous surface between the protrusions, which was also observed with AFM, revealing a smooth surface with a RMS roughness of ca. 6 nm and 7.5 nm for the 12 and 17 wt% support, respectively (**Table 1** and **Figure 4b**). Both TEM and AFM further validate the reliability of the ERD data, demonstrating that the marginal difference

in selective layer thickness does not correspond to a proportional change in the TFC membrane permeance.

All physicochemical characterizations suggest that the support contributes to the water permeance via a different phenomenon than just the selective layer formation and its properties. The influence of the support on the water permeance of the TFC membranes might therefore be explained by a previously reported phenomenon, the so-called support-induced funnel effect (**Figure 5**) [30,53,54]. The funnel effect refers to the effective pathway water must take through the thin selective layer, and the interface between the two distinct layers (*i.e.*, selective layer and support), to access an open pore in the support layer. The impact being that the support causes additional transport hinderance, due to partial blockage of flow by its dense fractions (*i.e.*, non-porous part), which is dependent on the porosity and pore size. The effective pathway for water through the selective layer until a pore of the support is reached will be shorter for high porosity supports. This work substantiates this framework as the porous supports caused higher water permeance of the respective TFC membrane (**Figure S5**), without compromising selectivity.

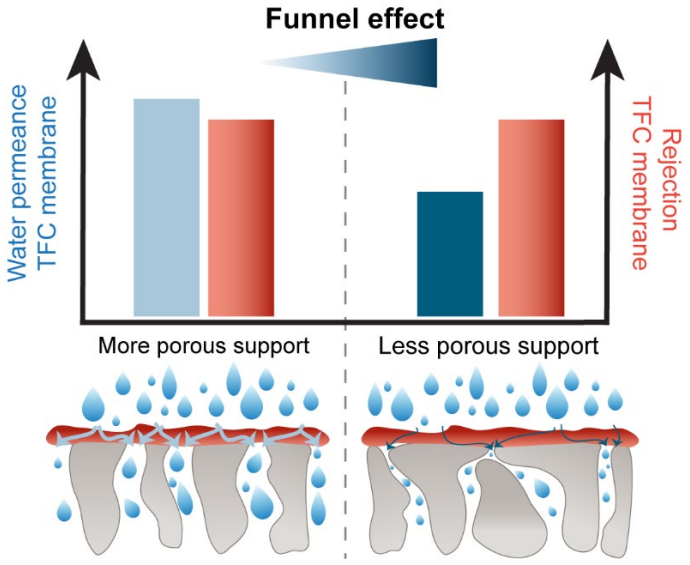

Figure 5. Schematic illustration of the SSP relationship of TFC membranes on top of a more porous support (left) and less porous support (right). Different supports result in PEE TFC membranes with similar rejections but different water permeances, where the least porous support causes lower permeances compared to a TFC membrane synthesized with a more porous support. The funnel effect is more severe for the less porous supports as the effective water pathway through the selective layer is longer until reaching the support pores.

3.1.2 Effect of support on XL-PEE selective layer

The additional post-treatment steps performed on the PEE membranes to achieve XL-PEE membranes caused a significant drop in water permeance below 9 L m^{-2} h^{-1} bar^{-1} and an increase in real NaCl rejection to around 65% for all XL-PEE TFC membranes (**Figure 6a**). For the entire PAN concentration range, the re-application of TMHD and EPON during the post-treatment step continues to show that there is no impact of the support on TFC membrane rejection, which is to be expected as the post-treatment steps are applied on top of the existing PEE layer, and are thus decoupled from the PAN support. In contrast to the rejection, water permeance of the XL-PEE membranes is affected by the support layer, until a certain threshold porosity and pore size are reached, after which its impact remains constant. This threshold appears to fall here between 12 wt% and 13 wt% PAN. According to the porosimetry measurements, this corresponds to a shift from approximately 86 nm to 65 nm.

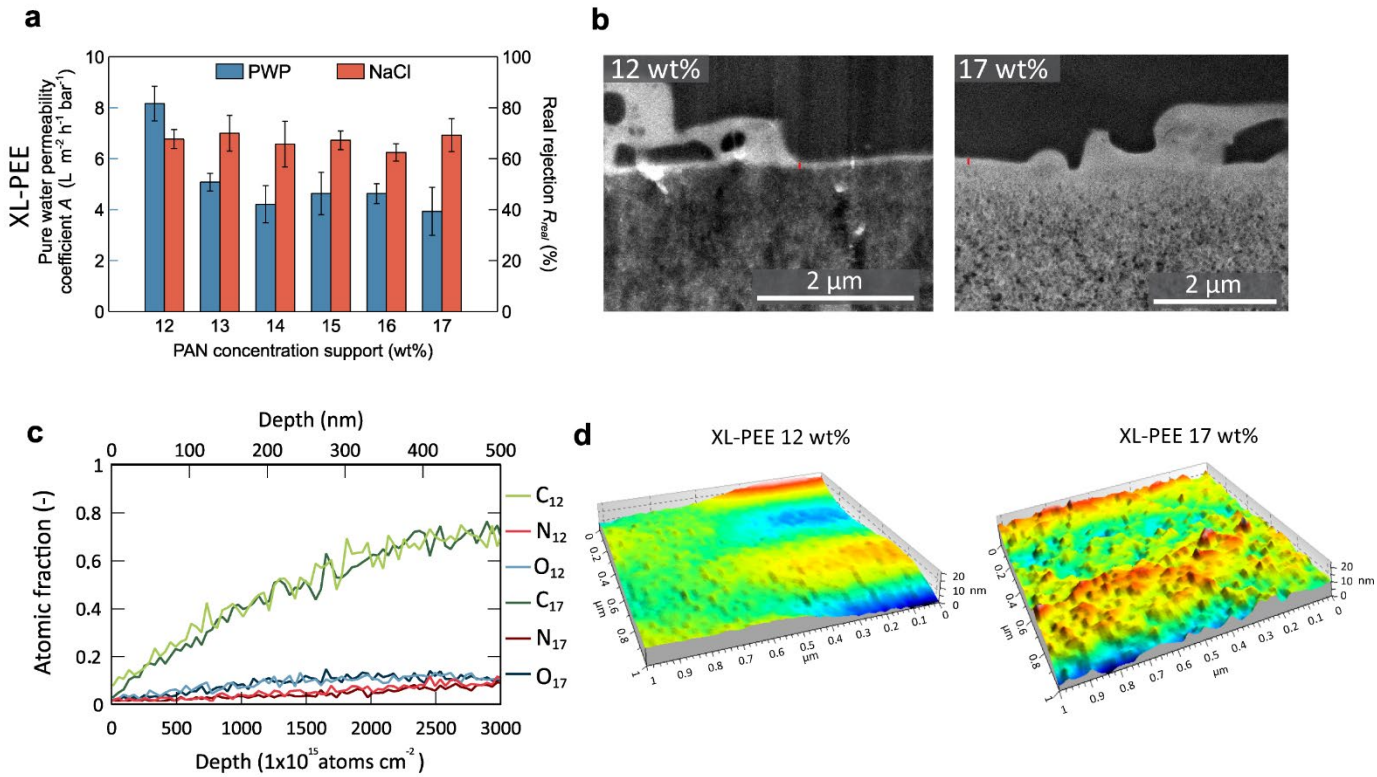

Figure 6. (a) Pure water permeance, expressed as pure water permeability coefficient *A*, and NaCl rejection of the XL-PEE TFC membranes as function of PAN concentration from which the support is cast. Experimental filtration conditions: 25° C, 10 bar, 5 mM aqueous NaCl solution. **(b)** TEM images of XL-PEE TFC membranes synthesized on 12 and 17 wt% PAN in NMP supports, with the red line indicating the XL-PEE selective layer. **(c)** ERD on the XL-PEE TFC membranes for the support layers synthesized with 12 and 17 wt% in NMP. **(d)** AFM images with a scan range of 1 × 1 µm^2 of the XL-PEE TFC membranes synthesized on 12 and 17 wt% PAN in NMP.

XPS confirms a similar degree of QA content in the selective layers (1.38 at.% for 12 wt% and 1.51 at.% for 17 wt% PAN support (**Table 1**), highlighting the prominent influence of the post-treatment procedure on positive charge incorporation, compared to the PEE selective layer (ca. 0.3 at.%). The similar rejection for the XL-PEE membranes is also corroborated by previous research that has indicated that, after achieving a certain mass density, the rejection mechanism becomes largely charge-based due to the positive QA groups incorporated in the selective layer, which originate from TMHD-incorporation in the network [23]. This is further mirrored in the similar selective layer morphology, as similar protrusions are found for the entire PAN support series (**Figure S6**).

Furthermore, the size of the FVEs in the selective layer on the 12 wt% PAN is only 0.4 Å smaller compared to that on the 17 wt% PAN, while their abundance is slightly higher (ca. 4.5%) (**Table 1** and **Figure S2**). Aside from densifying the polymer network, the post-treatment steps also cause the selective layer to become significantly thicker, as indicated by ERD and TEM (**Table 1** and **Figure 6c**), which is known to influence the permeance [55]. ERD measurements estimated the thickness of the XL-PEE layer to be 338 nm for the 12 wt% PAN and 411 nm for the 17 wt% PAN support, while TEM measurements indicate the same trend, but at lower absolute values (thickness of 121 nm and 143 nm, respectively). The overestimation of the actual thickness by ERD is mostly likely due to the impact on the recoil ions by the protrusions and the associated nanovoids encapsulated in the XL-PEE layer, clearly visible via TEM (**Figure S7**) [56]. While the surface area can also impact the membrane water permeance, the RMS roughness of each membrane (**Table 1** and **Figure 6d**) does not seem to correlate with the support porosity and pores nor with the observed water permeance.

Interestingly, the physicochemical data could not fully explain the discrepancy between the high water permeance of the XL-PEE TFC membranes on the 12 wt% PAN support and the constant water

permeances for the 13 – 17 wt% PAN support series (**Figure S5**). A possible hypothesis to explain this observation can again be found in the funnel effect (**Figure 5**) albeit less pronounced than for the PEE membranes. From the observed water permeance data, the funnel effect appears present until a threshold in support pore size and porosity is reached (*i.e.*, between 12 and 13 wt% PAN). At higher PAN concentrations, the impact of the support layer does not further impact water permeance of the XL-PEE membranes. In conclusion, the water permeance thus appears to be indirectly impacted by the support layer through the funnel effect until reaching a certain support pore size and porosity, rather than by other nanoscale characteristics of the selective layer (*i.e.*, FVE size, QA content, roughness and thickness). A similar observation was also found for the PEE membranes, further substantiating the importance of understanding the complex SSP relationships of TFC membranes.

3.2 Influence of casting solution solvent of support on TFC membrane performance

The choice of solvent in membrane casting has a significant impact on the phase separation process because it affects the solvent-non-solvent and polymer-solvent affinities, and thus the casting solution viscosity [57,58]. This in turn influences kinetics and thermodynamics of the system, hence the final support layer morphology, and related support permeance [59]. Indeed, clear differences in water permeance and cross-section morphology are observed when PAN supports are prepared from DMSO, NMP or DMF (**Figure 7a** and **d**). The permeance decreases from DMSO to NMP and finally to DMF (**Figure 7a**), as previously observed [60]. The DMSO-based supports contain a skin layer with large finger-like macrovoids that span the entire thickness, while the DMF and NMP-based supports contain small finger-like pores near the skin layer and larger macrovoids in the lower part (**Figure 7d**), in agreement with previous research [61–63]. Again, no significant impact of solvent annealing with toluene during IIP is observed on the permeances of these PAN support layers [56].

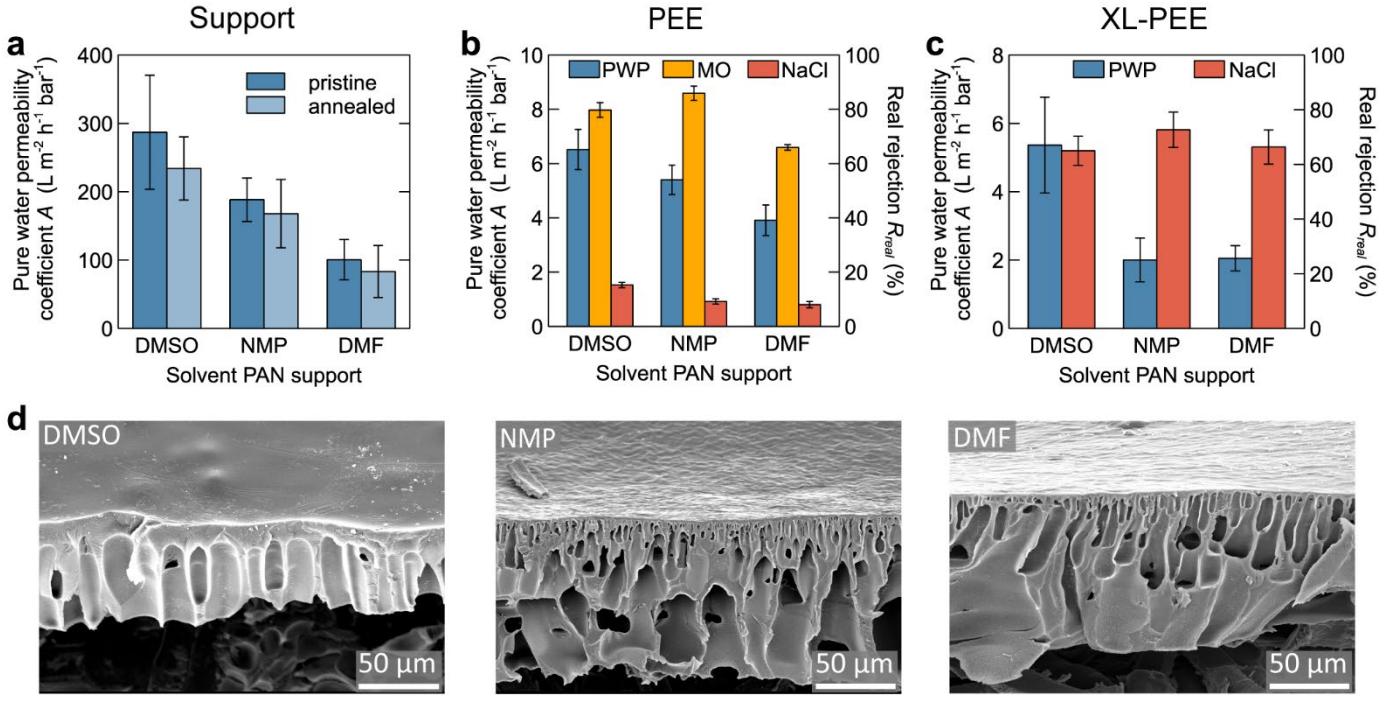

Figure 7. (a) Pure water permeance, expressed as pure water permeability coefficient, *A*, of pristine and annealed supports synthesized from 15 wt% PAN in different solvents (DMSO, NMP, DMF) (annealing was performed without the presence of the initiator and the epoxide monomer). **(b)** Pure water permeance, expressed as pure water permeability coefficient *A*, MO and NaCl rejection of the PEE TFC membranes as a function of the IPA-rinsed PAN supports synthesized with different solvents. **(c)** Pure water permeance, expressed as pure water permeability coefficient *A*, and NaCl rejection of the XL-PEE TFC membranes as a function of the IPA-rinsed PAN supports synthesized with different solvents. Experimental filtration conditions: 25 °C, 1 bar and MQ water for the support: 10 bar, 35 µM aqueous MO solution and 5 mM aqueous NaCl solution for the TFC membranes. **(d)** Cross-section SEM images of the support layers synthesized with different solvents.

In agreement with the results of the 12 – 17wt% PAN support, the water permeances of the PEE and XL-PEE TFC membranes, of which the supports were rinsed with a 25 v/v% IPA solution, positively correlate with the water permeance of the support: a more porous support leads to higher water permeances (**Figure 7**). In contrast, the support affects the MO rejection for the PEE membranes (**Figure 7b**) but does not seem to impact the NaCl rejection for the XL-PEE membranes (**Figure 7c**), as also observed for the PAN concentration series. Thus, the impact of the support properties is again clearly reflected in TFC membrane permeance, while the post-treatment step is predominantly determining the NaCl rejection.

Surprisingly, when the washing step with the IPA solution was not performed, the water permeance was strongly affected by the support and hence the related solvent used for NIPS (**Figure S8**). While DMSO, NMP and DMF are all polar aprotic solvents, an increase for DMSO and a decrease for NMP and DMF were observed for the TFC membranes after the IPA-wash step (**Table S7**). ATR-FTIR spectra show that the additional wash step of the support partially removes the residual solvent, which is trapped in the polymer matrix after phase inversion (**Figure S9**) [64]. Therefore, it is plausible that this observed trend is due to solvent clusters that are present in the unwashed support. The presence of solvent clusters can influence the selective layer formation and even induce blockage of water transport, and thus cause lower water permeances [65–67].

It is hypothesized that during IIP, when the support is brought into contact with the organic phase (*i.e.*, toluene), the support can swell, enabling the residual solvent to reach the interfacial reaction zone, and thereby possibly act as a co-solvent. More specifically, co-solvent assisted IP has been investigated previously for PA films, where it affected film formation by influencing the miscibility of the interface and thus the reaction zone, as well as the diffusion and solubility of the monomers [31,68–72]. Aside from the impact the residual solvent can have on the IIP, it can also affect the AROP mechanism itself. Indeed, DMSO is known, due to its high polarity, for promoting ion dissociation and chain transfer reactions, which in turn affect the final PEE network [73–75]. Hence, these observations and the performance of the TFC membranes clearly illustrate the complex interactions between the solvents (*i.e.*, solvent used during NIPS, IPA of the washing step, and toluene from IIP), the formed polymeric network, the interface and the support polymer chemistry, and require careful consideration in order to understand the complicated SSP relationships of these membranes.

4. Conclusions

This work illustrates the significant impact of the support on the performance and physicochemical properties of epoxide-based TFC membranes synthesized via IIP. By harmonizing the physicochemical properties of the PEE and XL-PEE selective layers with the experimentally obtained filtration results, a more fundamental understanding of transport through the TFC membrane was attained. The results of this study indicate that the support dictates water transport more than solute transport and dissimilarly affects the performance of the PEE and XL-PEE TFC membranes. The PEE selective layer formation via IIP is unaffected by the support synthesized with different PAN concentrations, as the selective layer thickness, roughness, FVE size and abundance, and QA content remain similar. The additional post-treatment steps of the PEE selective layer result in XL-PEE TFC membranes with a constant rejection of ca. 65% NaCl, which is again independent of the support layer. Hence, the selectivity of the PEE and XL-PEE TFC membranes is unaffected by support layers of different porosity and pore size, unlike conventional PA-based IP. In contrast to selectivity, the water permeance of both PEE (6 – 27 L m^{-2} h^{-1} bar^{-1}) and XL-PEE TFC membranes (4 – 8 L m^{-2} h^{-1} bar^{-1}) is significantly impacted by the support. This can partially be explained by the support-induced funnel effect, which describes the effective water pathway through TFC membranes until reaching the support pores. Support layer properties, such as pore size and porosity, are thus of paramount importance to overcome the water-salt perm-selectivity trade-off. In addition, the solvent used to prepare the support during the process of phase inversion is an additional parameter that strongly influences the performance of the TFC membranes. Residual solvent clusters still present in the support after phase inversion can act as a co-

solvent during IIP, thus affecting the interfacial properties and hence the polymerization. The obtained results highlight that optimization of the support layer and understanding its impact on the selective layer formation are key in tuning overall TFC membrane performance.

Data statement

Spectroscopic data and membrane performance data from this article is available in the KU Leuven research data repository: https://doi.org/10.48804/CKUNM8.

CRediT authorship contribution statement

Nathalie Lenaerts: Conceptualization, Data curation, Investigation, Methodology, Formal analysis, Validation, Visualization, Writing – original draft, Writing – review & editing. **Rhea Verbeke:** Conceptualization, Data curation, Methodology, Supervision, Validation, Writing – review & editing. **Douglas M. Davenport:** Conceptualization, Methodology, Supervision, Validation, Writing – review & editing. **Scout Caspers:** Data curation, Formal analysis, Investigation, Software, Writing – review & editing. **Samuel Eyley:** Data curation, Formal analysis, Software, Investigation, Writing – review & editing. **Karim-Alexandros Kantre:** Data curation, Formal analysis, Investigation, Software, Writing – review & editing. **Alexander Volodine:** Data curation, Formal analysis, Software, Writing – review & editing. **Ricardo Helm:** Data curation, Formal analysis, Investigation, Software, Writing – review & editing. **Maik Butterling:** Data curation, Formal analysis, Investigation, Software. **Maciej Oskar Liedke:** Data curation, Formal analysis, Investigation, Software. **Andreas Wagner:** Data curation, Formal analysis, Investigation, Software. **Wim Thielemans:** Funding acquisition, Resources. **Johan Meersschaut:** Funding acquisition, Resources, Writing – review & editing. **Marcel Dickmann:** Data curation, Formal analysis, Investigation, Software, Funding acquisition, Resources, Writing – review & editing. **Ivo F. J. Vankelecom:** Funding acquisition, Resources, Writing – review & editing.

Declaration of competing interest

The authors declare that they have no known competing financial interest or personal relationships that could have appeared to influence the work reported in this paper.

Acknowledgements

This work was funded in part by KU Leuven (C16/23/006 and VTI-23-00181) and by Research Foundation Flanders (G0C6623N, infrastructure projects AKUL13/19 and I000920N). N. L. would like to thank the Electron Microscopy Platform & Bio Imaging Core| VIB-KU Leuven Center for Brain and Disease Research| KU Leuven of the Department of Neurosciences. R. V. thanks the Research Foundation Flanders for her postdoctoral fellowship (1216222N). S. C. thanks the Research Foundation Flanders for his PhD fellowship (1SF9825N). S.E and W. T. thank KU Leuven (grants C14/23/093 and IBOF/21/105) and Research Foundation Flanders (grant S004624N) for funding.

Appendix. Supplementary materials

References

[1] M.A. Shannon, P.W. Bohn, M. Elimelech, J.G. Georgiadis, B.J. Mariñas, A.M. Mayes, Science and technology for water purification in the coming decades, Nature 452 (2008) 301–310. https://doi.org/10.1038/nature06599.

[2] M.S. Mauter, I. Zucker, F. Perreault, J.R. Werber, J.-H. Kim, M. Elimelech, The role of nanotechnology in tackling global water challenges, Nat Sustain 1 (2018) 166–175. https://doi.org/10.1038/s41893-018-0046-8.

[3] N. Shehata, D. Egirani, A.G. Olabi, A. Inayat, M.A. Abdelkareem, K.-J. Chae, E.T. Sayed, Membrane-based water and wastewater treatment technologies: Issues, current trends,

challenges, and role in achieving sustainable development goals, and circular economy, Chemosphere 320 (2023) 137993. https://doi.org/10.1016/j.chemosphere.2023.137993.
[4] M. Issaoui, S. Jellali, A.A. Zorpas, P. Dutournie, Membrane technology for sustainable water resources management: Challenges and future projections, Sustainable Chemistry and Pharmacy 25 (2022) 100590. https://doi.org/10.1016/j.scp.2021.100590.
[5] C. He, Z. Liu, J. Wu, X. Pan, Z. Fang, J. Li, B.A. Bryan, Future global urban water scarcity and potential solutions, Nat Commun 12 (2021) 4667. https://doi.org/10.1038/s41467-021-25026-3.
[6] Z. Wang, A. Deshmukh, Y. Du, M. Elimelech, Minimal and zero liquid discharge with reverse osmosis using low-salt-rejection membranes, Water Research 170 (2020) 115317. https://doi.org/10.1016/j.watres.2019.115317.
[7] M.J.T. Raaijmakers, N.E. Benes, Current trends in interfacial polymerization chemistry, Progress in Polymer Science 63 (2016) 86–142. https://doi.org/10.1016/j.progpolymsci.2016.06.004.
[8] V. Freger, G.Z. Ramon, Polyamide desalination membranes: Formation, structure, and properties, Progress in Polymer Science 122 (2021) 101451. https://doi.org/10.1016/j.progpolymsci.2021.101451.
[9] J.R. Werber, C.O. Osuji, M. Elimelech, Materials for next-generation desalination and water purification membranes, Nat Rev Mater 1 (2016) 1–15. https://doi.org/10.1038/natrevmats.2016.18.
[10] A. El Fadil, R. Verbeke, M. Kyburz, P. E M Aerts, I.F.J. Vankelecom, From academia to industry: Success criteria for upscaling nanofiltration membranes for water and solvent applications, Journal of Membrane Science 675 (2023) 121393. https://doi.org/10.1016/j.memsci.2023.121393.
[11] R. Verbeke, V. Gómez, I.F.J. Vankelecom, Chlorine-resistance of reverse osmosis (RO) polyamide membranes, Progress in Polymer Science 72 (2017) 1–15. https://doi.org/10.1016/j.progpolymsci.2017.05.003.
[12] G. Bargeman, Recent developments in the preparation of improved nanofiltration membranes for extreme pH conditions, Separation and Purification Technology 279 (2021) 119725. https://doi.org/10.1016/j.seppur.2021.119725.
[13] N. Daems, S. Milis, R. Verbeke, A. Szymczyk, P.P. Pescarmona, I.F.J. Vankelecom, High-performance membranes with full pH-stability, RSC Adv. 8 (2018) 8813–8827. https://doi.org/10.1039/C7RA13663C.
[14] S. Platt, M. Nyström, A. Bottino, G. Capannelli, Stability of NF membranes under extreme acidic conditions, Journal of Membrane Science 239 (2004) 91–103. https://doi.org/10.1016/j.memsci.2003.09.030.
[15] J. Lee, Y. Shin, C. Boo, S. Hong, Performance, limitation, and opportunities of acid-resistant nanofiltration membranes for industrial wastewater treatment, Journal of Membrane Science 666 (2023) 121142. https://doi.org/10.1016/j.memsci.2022.121142.
[16] M. Lenaerts, M. Thijs, R. Dhondt, C. Van Goethem, H.-Y. Chi, K.V. Agrawal, I. Vankelecom, G. Koeckelberghs, Development of tuneable polyamine top layer for nanofiltration with high stability in bleach and at extreme pHs, Journal of Membrane Science 693 (2024) 122341. https://doi.org/10.1016/j.memsci.2023.122341.
[17] A. Asadi Tashvigh, M.G. Elshof, N.E. Benes, Development of Thin-Film Composite Membranes for Nanofiltration at Extreme pH, ACS Appl. Polym. Mater. 3 (2021) 5912–5919. https://doi.org/10.1021/acsapm.1c01172.
[18] Z. Wang, R. Zhang, S. Zhang, W. Li, K. Zhi, Y. Su, Z. Jiang, Polyurea nanofiltration membranes with extreme-pH stability and high separation performance, Journal of Membrane Science 692 (2024) 122286. https://doi.org/10.1016/j.memsci.2023.122286.
[19] M.G. Elshof, W.M. De Vos, J. De Grooth, N.E. Benes, On the long-term pH stability of polyelectrolyte multilayer nanofiltration membranes, Journal of Membrane Science 615 (2020) 118532. https://doi.org/10.1016/j.memsci.2020.118532.

[20] S. Ilyas, N. Joseph, A. Szymczyk, A. Volodin, K. Nijmeijer, W.M. De Vos, I.F.J. Vankelecom, Weak polyelectrolyte multilayers as tunable membranes for solvent resistant nanofiltration, Journal of Membrane Science 514 (2016) 322–331. https://doi.org/10.1016/j.memsci.2016.04.073.
[21] R. Verbeke, M. Seynaeve, M. Bastin, D.M. Davenport, S. Eyley, W. Thielemans, G. Koeckelberghs, M. Elimelech, I.F.J. Vankelecom, The significant role of support layer solvent annealing in interfacial polymerization: The case of epoxide-based membranes, Journal of Membrane Science 612 (2020) 118438. https://doi.org/10.1016/j.memsci.2020.118438.
[22] R. Verbeke, W. Arts, E. Dom, M. Dickmann, W. Egger, G. Koeckelberghs, A. Szymczyk, I.F.J. Vankelecom, Transferring bulk chemistry to interfacial synthesis of TFC-membranes to create chemically robust poly(epoxyether) films, Journal of Membrane Science 582 (2019) 442–453. https://doi.org/10.1016/j.memsci.2019.02.016.
[23] R. Verbeke, D.M. Davenport, T. Stassin, S. Eyley, M. Dickmann, A.J. Cruz, P. Dara, C.L. Ritt, C. Bogaerts, W. Egger, R. Ameloot, J. Meersschaut, W. Thielemans, G. Koeckelberghs, M. Elimelech, I.F.J. Vankelecom, Chlorine-Resistant Epoxide-Based Membranes for Sustainable Water Desalination, Environ. Sci. Technol. Lett. 8 (2021) 818–824. https://doi.org/10.1021/acs.estlett.1c00515.
[24] M. Bastin, K. Bogaert, E. Dom, R. Verbeke, I.F.J. Vankelecom, Towards fully epoxy-based thin film composite membranes for solvent-resistant and solvent-tolerant nanofiltration, Journal of Membrane Science 683 (2023) 121813. https://doi.org/10.1016/j.memsci.2023.121813.
[25] M. Bastin, J. Raymenants, M. Thijs, A. Vananroye, G. Koeckelberghs, I.F.J. Vankelecom, Epoxy-based solvent-tolerant nanofiltration membranes prepared via non-solvent induced phase inversion as novel class of stable membranes, Journal of Membrane Science 626 (2021) 119206. https://doi.org/10.1016/j.memsci.2021.119206.
[26] A. El Fadil, E. Bull, M. Bastin, R. Verbeke, S. Rezaei Hosseinabadi, S. Eyley, W. Thielemans, K. Nijmeijer, I.F.J. Vankelecom, Polyethyleneimine-cured epoxy-based solvent tolerant nanofiltration membranes, Journal of Membrane Science 685 (2023) 121862. https://doi.org/10.1016/j.memsci.2023.121862.
[27] R. Verbeke, D.M. Davenport, C. Bogaerts, S. Eyley, W. Thielemans, I.F.J. Vankelecom, Epoxide-based TFC membranes with tunable performance in the tight nanofiltration range, Journal of Membrane Science Letters 3 (2023) 100054. https://doi.org/10.1016/j.memlet.2023.100054.
[28] F. Liu, L. Wang, D. Li, Q. Liu, B. Deng, A review: the effect of the microporous support during interfacial polymerization on the morphology and performances of a thin film composite membrane for liquid purification, RSC Advances 9 (2019) 35417–35428. https://doi.org/10.1039/C9RA07114H.
[29] Y.J. Lim, K. Goh, G.S. Lai, Y. Zhao, J. Torres, R. Wang, Unraveling the role of support membrane chemistry and pore properties on the formation of thin-film composite polyamide membranes, Journal of Membrane Science 640 (2021) 119805. https://doi.org/10.1016/j.memsci.2021.119805.
[30] L.E. Peng, Z. Yang, L. Long, S. Zhou, H. Guo, C.Y. Tang, A critical review on porous substrates of TFC polyamide membranes: Mechanisms, membrane performances, and future perspectives, Journal of Membrane Science 641 (2022) 119871. https://doi.org/10.1016/j.memsci.2021.119871.
[31] I. Nulens, A. Ben Zvi, I.F.J. Vankelecom, G.Z. Ramon, Re-thinking polyamide thin film formation: How does interfacial destabilization dictate film morphology?, Journal of Membrane Science 656 (2022) 120593. https://doi.org/10.1016/j.memsci.2022.120593.
[32] X. Li, Q. Li, W. Fang, R. Wang, W.B. Krantz, Effects of the support on the characteristics and permselectivity of thin film composite membranes, Journal of Membrane Science 580 (2019) 12–23. https://doi.org/10.1016/j.memsci.2019.03.003.
[33] A.K. Ghosh, E.M.V. Hoek, Impacts of support membrane structure and chemistry on polyamide–polysulfone interfacial composite membranes, Journal of Membrane Science 336 (2009) 140–148. https://doi.org/10.1016/j.memsci.2009.03.024.

[34] I. Nulens, R. Peters, R. Verbeke, D.M. Davenport, C. Van Goethem, B. De Ketelaere, P. Goos, K.V. Agrawal, I.F.J. Vankelecom, MPD and TMC supply as parameters to describe synthesis-morphology-performance relationships of polyamide thin film composite membranes, Journal of Membrane Science 667 (2023) 121155. https://doi.org/10.1016/j.memsci.2022.121155.
[35] X. Song, B. Gan, Z. Yang, C.Y. Tang, C. Gao, Confined nanobubbles shape the surface roughness structures of thin film composite polyamide desalination membranes, Journal of Membrane Science 582 (2019) 342–349. https://doi.org/10.1016/j.memsci.2019.04.027.
[36] X.-H. Ma, Z.-K. Yao, Z. Yang, H. Guo, Z.-L. Xu, C.Y. Tang, M. Elimelech, Nanofoaming of Polyamide Desalination Membranes To Tune Permeability and Selectivity, Environ. Sci. Technol. Lett. 5 (2018) 123–130. https://doi.org/10.1021/acs.estlett.8b00016.
[37] L.E. Peng, Q. Gan, Z. Yang, L. Wang, P.-F. Sun, H. Guo, H.-D. Park, C.Y. Tang, Deciphering the Role of Amine Concentration on Polyamide Formation toward Enhanced RO Performance, ACS EST Eng. 2 (2022) 903–912. https://doi.org/10.1021/acsestengg.1c00418.
[38] Y. Du, L. Wang, A. Belgada, S.A. Younssi, J. Gilron, M. Elimelech, A mechanistic model for salt and water transport in leaky membranes: Implications for low-salt-rejection reverse osmosis membranes, Journal of Membrane Science 678 (2023) 121642. https://doi.org/10.1016/j.memsci.2023.121642.
[39] O. Peer-Haim, I. Shefer, P. Singh, O. Nir, R. Epsztein, The Adverse Effect of Concentration Polarization on Ion–Ion Selectivity in Nanofiltration, Environ. Sci. Technol. Lett. 10 (2023) 363–371. https://doi.org/10.1021/acs.estlett.3c00124.
[40] C.L. Ritt, T. Stassin, D.M. Davenport, R.M. DuChanois, I. Nulens, Z. Yang, A. Ben-Zvi, N. Segev-Mark, M. Elimelech, C.Y. Tang, G.Z. Ramon, I.F.J. Vankelecom, R. Verbeke, The open membrane database: Synthesis–structure–performance relationships of reverse osmosis membranes, Journal of Membrane Science 641 (2022) 119927. https://doi.org/10.1016/j.memsci.2021.119927.
[41] M.P. Seah, Simple universal curve for the energy-dependent electron attenuation length for all materials, Surface and Interface Analysis 44 (2012) 1353–1359. https://doi.org/10.1002/sia.5033.
[42] M.P. Seah, A system for the intensity calibration of electron spectrometers, Journal of Electron Spectroscopy and Related Phenomena 71 (1995) 191–204. https://doi.org/10.1016/0368-2048(94)02275-5.
[43] A. Wagner, M. Butterling, M.O. Liedke, K. Potzger, R. Krause-Rehberg, Positron annihilation lifetime and Doppler broadening spectroscopy at the ELBE facility, in: Newport News, VA, USA, 2018: p. 040003. https://doi.org/10.1063/1.5040215.
[44] E. Hirschmann, M. Butterling, U.H. Acosta, M.O. Liedke, A.G. Attallah, P. Petring, M. Görler, R. Krause-Rehberg, A. Wagner, A new system for real-time data acquisition and pulse parameterization for digital positron annihilation lifetime spectrometers with high repetition rates, J. Inst. 16 (2021) P08001. https://doi.org/10.1088/1748-0221/16/08/P08001.
[45] R. Helm, J. Lehtonen, M. Mayerhofer, J. Mitteneder, W. Egger, R. Verbeke, P. Sperr, G. Dollinger, M. Dickmann, Positron-annihilation lifetime spectroscopy with in-situ control of temperature, pressure and atmosphere to determine the free-volume of soft materials, Nuclear Instruments and Methods in Physics Research Section B: Beam Interactions with Materials and Atoms 549 (2024) 165263. https://doi.org/10.1016/j.nimb.2024.165263.
[46] ISO 25178-2:2012(en), Geometrical product specifications (GPS) — Surface texture: Areal — Part 2: Terms, definitions and surface texture parameters, (n.d.). https://www.iso.org/obp/ui/#iso:std:iso:25178:-2:ed-1:v1:en (accessed April 17, 2024).
[47] C. Klaysom, S. Hermans, A. Gahlaut, S. Van Craenenbroeck, I.F.J. Vankelecom, Polyamide/Polyacrylonitrile (PA/PAN) thin film composite osmosis membranes: Film optimization, characterization and performance evaluation, Journal of Membrane Science 445 (2013) 25–33. https://doi.org/10.1016/j.memsci.2013.05.037.

[48] Z. Yang, H. Guo, C.Y. Tang, The upper bound of thin-film composite (TFC) polyamide membranes for desalination, Journal of Membrane Science 590 (2019) 117297. https://doi.org/10.1016/j.memsci.2019.117297.
[49] A. Vazquez, D. Bentaleb, R.J.J. Williams, Curing of diepoxides with tertiary amines: Influence of temperature and initiator concentration on polymerization rate and glass transition temperature, Journal of Applied Polymer Science 43 (1991) 967–976. https://doi.org/10.1002/app.1991.070430514.
[50] J. Wang, D.S. Dlamini, A.K. Mishra, M.T.M. Pendergast, M.C.Y. Wong, B.B. Mamba, V. Freger, A.R.D. Verliefde, E.M.V. Hoek, A critical review of transport through osmotic membranes, Journal of Membrane Science 454 (2014) 516–537. https://doi.org/10.1016/j.memsci.2013.12.034.
[51] T. Fujioka, N. Oshima, R. Suzuki, W.E. Price, L.D. Nghiem, Probing the internal structure of reverse osmosis membranes by positron annihilation spectroscopy: Gaining more insight into the transport of water and small solutes, Journal of Membrane Science 486 (2015) 106–118. https://doi.org/10.1016/j.memsci.2015.02.007.
[52] X. Chen, R. Verbeke, C. Boo, M. Dickmann, W. Egger, K. Ndamage, I.F.J. Vankelecom, N.Y. Yip, Elucidating the Roles of Polyamide Layer Structural Properties in the Permeability–Selectivity Tradeoff Governing Aqueous Separations, ACS EST Eng. 2 (2022) 1857–1870. https://doi.org/10.1021/acsestengg.2c00103.
[53] Y. Qian, H. Li, J. Lu, D. Lu, H. Jin, Z. Xia, Z. Yao, J. Wang, L. Zhang, C.Y. Tang, Inhibiting Polyamide Intrusion of Thin Film Composite Membranes: Strategies and Environmental Implications, Environ. Sci. Technol. 57 (2023) 10860–10869. https://doi.org/10.1021/acs.est.3c02666.
[54] S. Mohammed, J. Aburabie, R. Hashaikeh, Facile morphological tuning of thin film composite membranes for enhanced desalination performance, Npj Clean Water 6 (2023) 1–12. https://doi.org/10.1038/s41545-023-00271-9.
[55] C. Ji, Z. Zhai, C. Jiang, P. Hu, S. Zhao, S. Xue, Z. Yang, T. He, Q.J. Niu, Recent advances in high-performance TFC membranes: A review of the functional interlayers, Desalination 500 (2021) 114869. https://doi.org/10.1016/j.desal.2020.114869.
[56] R. Verbeke, A. Bergmaier, S. Eschbaumer, H. Mariën, G. Dollinger, I.F.J. Vankelecom, Full elemental depth-profiling with nanoscale resolution: The potential of Elastic Recoil Detection (ERD) in membrane science, Journal of Membrane Science 572 (2019) 102–109. https://doi.org/10.1016/j.memsci.2018.10.045.
[57] A.K. Hołda, I.F.J. Vankelecom, Understanding and guiding the phase inversion process for synthesis of solvent resistant nanofiltration membranes, Journal of Applied Polymer Science 132 (2015). https://doi.org/10.1002/app.42130.
[58] P. Vandezande, X. Li, L.E.M. Gevers, I.F.J. Vankelecom, High throughput study of phase inversion parameters for polyimide-based SRNF membranes, Journal of Membrane Science 330 (2009) 307–318. https://doi.org/10.1016/j.memsci.2008.12.068.
[59] G.R. Guillen, Y. Pan, M. Li, E.M.V. Hoek, Preparation and Characterization of Membranes Formed by Nonsolvent Induced Phase Separation: A Review, Ind. Eng. Chem. Res. 50 (2011) 3798–3817. https://doi.org/10.1021/ie101928r.
[60] H. Lohokare, Y. Bhole, S. Taralkar, U. Kharul, Poly(acrylonitrile) based ultrafiltration membranes: Optimization of preparation parameters, Desalination 282 (2011) 46–53. https://doi.org/10.1016/j.desal.2011.04.009.
[61] I.-C. Kim, H.-G. Yun, K.-H. Lee, Preparation of asymmetric polyacrylonitrile membrane with small pore size by phase inversion and post-treatment process, Journal of Membrane Science 199 (2002) 75–84. https://doi.org/10.1016/S0376-7388(01)00680-9.
[62] A.A. Yushkin, M.N. Efimov, A.A. Vasilev, Yu.G. Bogdanova, V.D. Dolzhikova, G.P. Karpacheva, A.V. Volkov, Modification of polyacrylonitrile membranes by incoherent IR radiation, Pet. Chem. 57 (2017) 341–346. https://doi.org/10.1134/S0965544117040089.

[63] W. Yang, Z. Wang, Y. Zhou, X. Ye, L. Shi, L. Cheng, N. Chen, W. Dong, Q. Zhang, X. Zhang, Study on the control of pore sizes of membranes using chemical methods Part IV. The role of organic acids, Desalination 324 (2013) 57–64. https://doi.org/10.1016/j.desal.2013.06.002.
[64] N. Kizildag, N. Ucar, A. Onen, I. Karacan, Polyacrylonitrile/polyaniline composite nano/microfiber webs produced by different dopants and solvents, Journal of Industrial Textiles 46 (2016) 787–808. https://doi.org/10.1177/1528083715598654.
[65] A. El Fadil, S. Rezaei Hosseinabadi, R. De Oliveira Silva, D. Sakellariou, K. Nijmeijer, I.F.J. Vankelecom, Strong impact of exposure to water/solvent mixtures on permeance of nanofiltration membranes, Journal of Membrane Science 699 (2024) 122651. https://doi.org/10.1016/j.memsci.2024.122651.
[66] H. Fan, J. He, M. Heiranian, W. Pan, Y. Li, M. Elimelech, The physical basis for solvent flow in organic solvent nanofiltration, Science Advances 10 (2024) eado4332. https://doi.org/10.1126/sciadv.ado4332.
[67] Q.T. Nguyen, E. Favre, Z.H. Ping, J. Néel, Clustering of solvents in membranes and its influence on membrane transport properties, Journal of Membrane Science 113 (1996) 137–150. https://doi.org/10.1016/0376-7388(95)00219-7.
[68] R.H. Hailemariam, J.-S. Choi, M.M. Damtie, H. Rho, K.-D. Park, J. Lee, Y.C. Woo, Enhancing performances of polyamide thin film composite membranes via *co*-solvent assisted interfacial polymerization, Desalination 524 (2022) 115481. https://doi.org/10.1016/j.desal.2021.115481.
[69] J.A.D. Marquez, M.B.M.Y. Ang, B.T. Doma, S.-H. Huang, H.-A. Tsai, K.-R. Lee, J.-Y. Lai, Application of cosolvent-assisted interfacial polymerization technique to fabricate thin-film composite polyamide pervaporation membranes with PVDF hollow fiber as support, Journal of Membrane Science 564 (2018) 722–731. https://doi.org/10.1016/j.memsci.2018.07.084.
[70] S.-Y. Kwak, S.G. Jung, S.H. Kim, Structure-Motion-Performance Relationship of Flux-Enhanced Reverse Osmosis (RO) Membranes Composed of Aromatic Polyamide Thin Films, Environ. Sci. Technol. 35 (2001) 4334–4340. https://doi.org/10.1021/es010630g.
[71] T. Kamada, T. Ohara, T. Shintani, T. Tsuru, Optimizing the preparation of multi-layered polyamide membrane via the addition of a co-solvent, Journal of Membrane Science 453 (2014) 489–497. https://doi.org/10.1016/j.memsci.2013.11.028.
[72] T. Kamada, T. Ohara, T. Shintani, T. Tsuru, Controlled surface morphology of polyamide membranes via the addition of co-solvent for improved permeate flux, Journal of Membrane Science 467 (2014) 303–312. https://doi.org/10.1016/j.memsci.2014.03.072.
[73] P. Dreier, R. Matthes, R.D. Barent, S. Schüttner, A.H.E. Müller, H. Frey, In Situ Kinetics Reveal the Influence of Solvents and Monomer Structure on the Anionic Ring-Opening Copolymerization of Epoxides, Macromolecular Chemistry and Physics 224 (2023) 2200209. https://doi.org/10.1002/macp.202200209.
[74] A.-L. Brocas, C. Mantzaridis, D. Tunc, S. Carlotti, Polyether synthesis: From activated or metal-free anionic ring-opening polymerization of epoxides to functionalization, Progress in Polymer Science 38 (2013) 845–873. https://doi.org/10.1016/j.progpolymsci.2012.09.007.
[75] K.S. Kazanskii, A.A. Solovyanov, S.A. Dubrovsky, Some remarks to the kinetics of anionic polymerization of ethylene oxide in dimethyl sulfoxide, Die Makromolekulare Chemie 179 (1978) 969–973. https://doi.org/10.1002/macp.1978.021790411.